



# 1 **A subgrid method for the linear inertial equations of a compound** 2 **flood model**

3 Maarten van Ormondt<sup>1</sup>, Tim Leijnse<sup>2,3</sup>, Roel de Goede<sup>2</sup>, Kees Nederhoff<sup>1</sup>, Ap van Dongeren<sup>2,4</sup>

4 <sup>1</sup> Deltares USA, 8601 Georgia Ave, Silver Spring, MD 20910, USA

5 <sup>2</sup> Marine and Coastal Management, Deltares, Boussinesqweg 1, Delft, 2629 HV, The Netherlands

6 <sup>3</sup> Institute for Environmental Studies (IVM), Vrije Universiteit Amsterdam, De Boelelaan 1111, 1081 HV Amsterdam, The  
7 Netherlands.

8 <sup>4</sup> IHE Delft, Water Science and Engineering Dept, Westvest 7, 2611 AX Delft, The Netherlands

9 *Correspondence to:* Kees Nederhoff ([kees.nederhoff@deltares-usa.us](mailto:kees.nederhoff@deltares-usa.us))

10 **Keywords.** Hydrodynamic modeling, subgrid, Linear Inertial Equations, compound flooding, SFINCS

11

12 **Abstract.** Accurate flood risk assessments and early warning systems are needed to protect and prepare people in coastal areas  
13 from storms. In order to provide this information efficiently and on time, computational costs need to be kept as low as  
14 possible. Reduced-complexity models using linear inertial equations and subgrid approaches have been used previously to  
15 achieve this goal. In this paper, for the first time, we developed a subgrid approach for the Linear Inertial Equations (LIE) that  
16 account for bed level and friction variations. We implemented this method in the SFINCS model. Pre-processed lookup tables  
17 that correlate water levels with hydrodynamic quantities make more precise simulations with lower computational costs  
18 possible. These subgrid corrections have undergone validation through a variety of conceptual and real-world application  
19 scenarios, including analyses of hurricane hazards and tidal fluctuations. We demonstrate that the subgrid corrections for  
20 Linear Inertial Equations significantly improve model accuracy while utilizing the same resolution without subgrid corrections.  
21 Moreover, coarser model resolutions with subgrid corrections can provide the same accuracy as finer resolutions without  
22 subgrid corrections. Limitations are discussed, for example, when grids do not adequately resolve river meanders, fluxes can  
23 be overestimated. Our findings show that subgrid corrections are an invaluable asset for hydrodynamic modelers striving to  
24 achieve a balance between accuracy and efficiency.



## 25 1 Introduction

26 With hundreds of millions of people living in areas with an elevation of less than 10 meters above sea level (McGranahan et  
27 al, 2007), coastal zone flooding has large consequences for casualties and damage to real estate and infrastructure. To protect  
28 and mitigate flood damages and loss of life, a priori risk assessments may inform decision makers in what locations and under  
29 what circumstances flooding occurs, and what interventions to take. Furthermore, flood early warning systems provide  
30 information based on which evacuation of citizens can take place to save lives. Both the risk assessments and early warning  
31 systems should provide as accurate as possible information so as not to give false warnings or needlessly over or underestimate  
32 the extent and cost of interventions.

33

34 For flood warnings, this means that simple bathtub approaches, where a peak water level is imposed on an area's topography,  
35 do not suffice. They may overestimate the flood intensity because the surge hydrograph is not taken into account (Vousdoukas  
36 et al., 2016), or underestimate it due to lacking physics (e.g. wave effects, Didier et al., 2020) or lacking inputs such as  
37 roughness effects which would impede flow (Ramirez et al., 2016). Therefore, for a more accurate flood estimate, the dynamic  
38 aspects of floods such as the duration of an event, and the path that flood waters take should be considered. Furthermore, the  
39 compound nature of coastal area floods, which may be caused by marine surges, wave overtopping, coastal river discharges,  
40 and local rainfall needs to be taken into account. These dynamics and processes may be resolved using process-based numerical  
41 models which are based on the conservation of mass and momentum. However, classical full-physics models (ADCIRC;  
42 Luettich et al., 1992, Delft3D-FLOW; Lesser et al., 2004, MIKE; Warren and Bach, 1992 or SOBEK; Stelling et al., 1998) are  
43 computationally expensive, which limits their application for large areas and high resolution, and the exploration of  
44 uncertainties in flooding due to uncertain inputs.

45

46 To that end, reduced-complexity models have been developed and applied in riverine settings and coastal applications.  
47 Examples include, among others, the LISFLOOD(-FP) model by Bates et al. (2010) and the SFINCS (Super-Fast INundation  
48 of CoastS) model by Leijnse et al. (2021)). These models solve only the essential terms in the momentum equations using a  
49 simple numerical scheme and are as a consequence orders of magnitude faster than the conventional models. Still, the number  
50 of simulations that can be run is limited, as the numerical scheme is explicit and therefore strongly influenced by the spatial  
51 grid size (and associated time step).

52

53 One way to further increase the computational speed is to apply a subgrid approach which makes use of the assumption that  
54 water level gradients are typically much smaller than topographic gradients. Defina (2000) presented shallow water equations  
55 with mass conservation corrections to account for wetting and drying areas, and corrections to the momentum equations to  
56 account for varying velocities. Casulli (2009) introduced a dual-grid approach with a higher resolution grid for the bathymetry  
57 and a lower resolution grid for the hydrodynamics where the depth and cross-sectional area were computed using the higher-



58 resolution grid and stored in lookup tables which were used to evaluate the water levels on the lower resolution grid. Volp et  
59 al. (2013) extended Casulli's approach to finite volumes and incorporated a subgrid-based method to compute advection and  
60 bottom friction under the assumptions of locally uniform flow direction and friction slope. Sehili et al. (2014) showed that a  
61 subgrid approach could save an order of magnitude of computational cost without major accuracy loss in estuarine modeling.  
62 For coastal storm surge applications, Kennedy et al. (2019) developed a refined set of equations incorporating extra terms  
63 derived from an upscaling technique. These additional terms, emerging from the averaging of shallow water equations, account  
64 for the integral properties of fine-scale bathymetry, topography, and flow dynamics. This process is similar to how Boussinesq  
65 approximations are used for turbulence closure in Navier-Stokes models and involves using coarse-scale variables, such as  
66 averaged fluid velocity, to represent these fine-scale integrals. They showed the improved performance of their model for the  
67 case of tidal flooding in a small bay. Woodruff et al. (2021) extended this analysis to a case of storm surge with realistic  
68 atmospheric forcing and reported a speedup of ADCIRC with a factor of 10-50. Similarly, Begmohammadi et al. (2023)  
69 adapted the numerical implementation of the real-time forecasting model SLOSH (Jelesnianski and Chester, 1992) to improve  
70 inundation performance in a coastal region with narrow channels. Woodruff et al. (2023) scaled up these approaches to the  
71 entire South Atlantic Bight and showed improved performance of a subgrid model to a conventional high-resolution model for  
72 Hurricane Matthew (2016).

73

74 While these advances have led to great improvements in estuarine and storm surge modeling, the assumption of hydraulic  
75 connectivity of subgrid cells remains a challenge. To that end, Begmohammadi et al. (2021) removed the artifact of flows  
76 occurring through catchment boundaries that are not resolved in a subgrid approach by restricting flow to a predetermined  
77 path. Rong et al. (2023) introduced a new diffusive scheme in the existing subgrid channel approach to better model flood  
78 routing in rivers and adjacent flood plains. Yu and Lane (2011) applied a subgrid approach to resolve the roughness effects of  
79 small-scale structural elements in river floodplain cases, based on the method by Yu and Lane (2006) and applied a storage  
80 correction to the coarser scale flow grid based on the higher-resolution topographic information accounting for cell blockage  
81 and conveyance effects.

82

83 However, none of these efforts combined a reduced-complexity model with a subgrid approach that accounts for bed level and  
84 friction variations for efficient compound flood modeling. In this paper, we explore a subgrid approach for the Linear Inertial  
85 Equations (Bates et al., 2010) that are used in the SFINCS model (Leijnse et al., 2021). All model results were obtained with  
86 the SFINCS 'Cauberg' release from November 2023 which is available as open-source code on GitHub and via  
87 <https://www.deltares.nl/en/software-and-data/products/sfincs> (van Ormondt et al., 2023). Computational speed is determined  
88 by running the simulations on an Intel core I9 10980XE CPU.

89



90 The paper is organized as follows: we start with the governing equation in SFINCS, and a description of the new subgrid  
91 approach (Section 2). We then demonstrate the accuracy of the subgrid method for some conceptual cases (Section 3). In  
92 Section 4, the subgrid method is verified against the default SFINCS results and observed data for two real-world cases: tidal  
93 propagation at the St. Johns River (Florida, USA) and the flooding during Hurricane Harvey (Houston, USA). The findings  
94 are discussed in Section 5 and our conclusions are presented in Section 6.

## 95 2 Model description

### 96 2.1 SFINCS governing equations

97 The SFINCS model solves the shallow-water equations on a regular, staggered Arakawa-C grid. Its governing equations are  
98 based on the Linear Inertial Equations (LIEs; Bates et al., 2010). In particular, the volumetric flow rate per unit width at the  
99 interface between adjacent cells in the  $x$  direction for the current time step is computed with Equation 1:

$$100 \quad q_u^{t+\Delta t} = \frac{q_u^t - g\Delta t h_u \frac{\Delta z}{\Delta x} + F\Delta t}{1 + g\Delta t n^2 |q_u^t| / h_u^{7/3}} \quad (1)$$

101 where  $q_u^t$  is the flow rate at the previous time step,  $h_u$  and  $\Delta z/\Delta x$  are the water depth and water level gradient at the cell interface  
102  $u$ ,  $g$  is the acceleration constant,  $n$  is the Manning's  $n$  roughness and  $\Delta t$  is the time step. The water depth  $h_u$  at the cell interface  
103 is computed in SFINCS as the difference between the maximum water level in the two adjacent cells and the maximum bed  
104 level in these cells. For the sake of brevity, additional forcing terms, such as wind drag, barometric pressure gradients, and the  
105 advection term, are represented in the combined term  $F$ .

106

107 The mass continuity equation reads:

$$108 \quad z_s^{t+\Delta t} = z_s^t + \Delta t \left( \frac{q_{u\ m-1,n}^t - q_{u\ m,n}^t}{\Delta x} + \frac{q_{v\ m,n-1}^t - q_{v\ m,n}^t}{\Delta y} + \frac{S_{m,n}}{\Delta x \Delta y} \right) \quad (2)$$

109 where  $z_s$  is the water level in a grid cell (with index  $m$  in  $x$ -direction,  $n$  in  $y$ -direction), and  $S_{m,n}$  is an (optional) source term in  
110  $\text{m}^3/\text{s}$  (e.g. to represent precipitation or a user-defined point source). In the remainder of this document, formulations will often  
111 be presented in the  $x$  direction, with the  $y$  direction treated analogously (with cell interface  $v$ ).

112

113 SFINCS uses a first-order explicit backward in time with a first-order central difference approximation of the spatial derivatives  
114 (BTCS-scheme).



## 115 2.2 Subgrid corrections in the momentum equation

116 The goal of the subgrid approach is to compute flooding in a computationally efficient way using larger grids while retaining  
117 information of the higher-resolution elevation data. This is achieved by adjusting the conveyance depth  $h_u$  and Manning's  
118 roughness  $n$  in Equation 1 based on the local water level  $z_u$  and the subgrid topography and roughness so that the unit discharge  
119  $q_u$  through a cell interface equals the average of the unit discharge of the subgrid pixels within the considered velocity point.  
120 An important assumption here is that the water level within the velocity point is constant, and therefore equal for all subgrid  
121 pixels. If the subgrid topography is known, and we assume that the water level  $z_u$  is constant for all subgrid pixels in the  
122 velocity point, then representative values for  $h_u$  and  $n$  (as well as the wet fraction  $\varphi$ ) can be computed as a function of  $z_u$  and  
123 stored in look-up tables for each velocity point. During a simulation, these look-up tables are queried at each time step to  
124 provide representative values for  $h_u$ ,  $n$ , and  $\varphi$ . This Section explains the theory behind the subgrid approach for the LIEs. The  
125 following sections describe the practical generation of the subgrid tables, and how these are queried during a SFINCS  
126 simulation.

127

128 Following the notation of Kennedy et al. (2019), for a quantity  $Q$ , hydrodynamic variables coarsened to the grid scale are  
129 defined as:

$$130 \quad \langle Q \rangle_G = \frac{1}{A} \iint_{A_W} Q dA \quad (3)$$

131 where  $A_W$  is the wet portion of the grid cell area  $A$ . This will be called the “grid average” and is denoted with subscript “G”.

132

133 On the other hand, the “wet average” of  $Q$ , denoted with subscript “W” is:

$$134 \quad \langle Q \rangle_W = \frac{1}{A_W} \iint_{A_W} Q dA \quad (4)$$

135

136 With the wet average area is defined as:

$$137 \quad A_W = \varphi A \quad (5)$$

138 where  $\varphi$  is the wet fraction of the cell area, then for hydrodynamic quantity  $Q$ :

$$139 \quad \langle Q \rangle_G = \varphi \langle Q \rangle_W \quad (6)$$

140

141 The LIEs in their subgrid form using wet average quantities can be defined as:

$$142 \quad \langle q_u \rangle_W^{t+\Delta t} = \frac{\langle q_u \rangle_W^t - g \Delta t \langle H_u \rangle_W \frac{\Delta z}{\Delta x} + F \Delta t}{1 + g \Delta t n_{u,W}^2 |\langle q_u \rangle_W^t| / \langle H_u \rangle_W^{7/3}} \quad (7)$$



143 where  $\langle q_u \rangle_W$  and  $\langle H_u \rangle_W$  are the wet average unit discharge and water depth, respectively, and  $n_{u,W}$  is the Manning's  $n$   
 144 coefficient adjusted for subgrid variations.

145

146 The expression for  $n_{u,W}$  can be derived by considering Manning's equation for open channel flow :

$$147 \quad \langle q_u \rangle_W = \sqrt{i} \frac{\langle H_u \rangle_W^{5/3}}{n_{u,W}} \quad (8)$$

148 where  $i$  is the water level slope  $\frac{\Delta z_s}{\Delta x}$ . In case of a stationary current and in the absence of external forcing, the subgrid form of  
 149 the LIEs reverts to Equation 8. Consider now a velocity point with  $N$  subgrid pixels, each with its own bed level  $z_{b,k}$  and  
 150 roughness  $n_k$  (see Figure 1 and Figure 2). For a water level  $z_u$ , the water depth in each pixel is  $h_k = \max(z_u - z_{b,k}, 0)$ . The wet  
 151 average unit discharge of the subgrid pixels within the velocity point is:

$$152 \quad \langle q_u \rangle_W = \frac{1}{\varphi_u N} \sqrt{i} \sum_{k=1}^N \frac{h_k^{5/3}}{n_k} \quad (9)$$

153 where  $\varphi_u N$  is the number of wet pixels. Equation 9 can also be written as:

$$154 \quad \langle q_u \rangle_W = \sqrt{i} \frac{\langle H_u \rangle_W^{5/3}}{n} \quad (10)$$

155

156 Substituting Equation 10 into Equation 8 yields the expression for  $n_{u,W}$  (Equation 11):

$$157 \quad n_{u,W} = \frac{\langle H_u \rangle_W^{5/3}}{\langle \frac{H_u}{n} \rangle_W} \quad (11)$$

158

159 The subgrid form of the LIEs (Equations 7 and 11) can alternatively be expressed with grid average quantities. The SFINCS  
 160 model uses these to solve the momentum balance, rather than the wet average quantities described above. Although somewhat  
 161 less intuitive, using grid average quantities has a few practical advantages that will be discussed in the next section. To write  
 162 the subgrid form of the LIEs using grid average quantities we simply substitute  $\langle q_u \rangle_W$  with  $\langle q_u \rangle_G / \varphi_u$  and  $\langle H_u \rangle_W$  with  
 163  $\langle H_u \rangle_G / \varphi_u$  in Equation 7:

$$164 \quad \langle q_u \rangle_G^{t+\Delta t} = \frac{\langle q_u \rangle_G^t - g \Delta t \langle H_u \rangle_G \frac{\Delta z}{\Delta x} + \varphi_u F \Delta t}{1 + g \Delta t n_u^2 |\langle q_u \rangle_G^t| / \langle H_u \rangle_G^{7/3}} \quad (12)$$

165 where  $n_u$  is  $\varphi_u^{2/3} n_{u,W}$ .

166

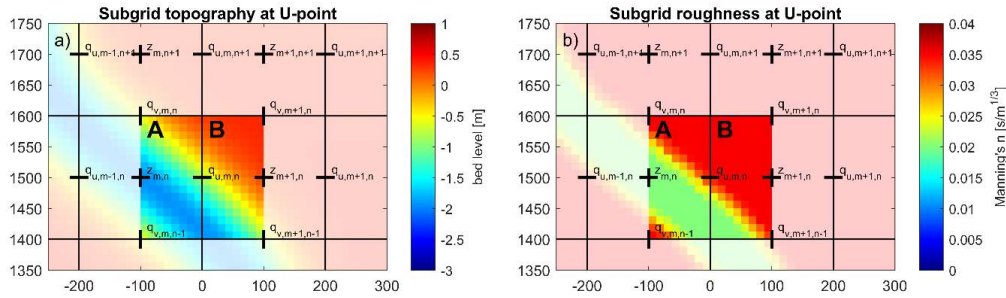
167 Using the same logic as for Equation 11,  $n_u$  (hereafter called the representative roughness) can also be written as:



168

$$n_u = \frac{\langle H_u \rangle_G^{5/3}}{\langle \frac{H_u}{n} \rangle_G^{5/3}} \quad (13)$$

169 For a known subgrid topography, and assuming a constant water level  $z_u$  for all subgrid pixels in the velocity point,  $\langle H_u \rangle_G$ ,  $n_u$ ,  
 170 and  $\varphi_u$  can be stored in look-up tables as a function of  $z_u$ . The generation of such tables is a pre-processing step that occurs  
 171 only once when the model is set up, and is not repeated in the computational loop. First, a subgrid is generated that has the  
 172 same orientation as the coarser hydrodynamic grid and a higher resolution. The level of refinement of the subgrid is an even  
 173 integer and is typically chosen such that the subgrid resolution roughly equals that of the digital elevation model (DEM). Next,  
 174 the subgrid model bathymetry is generated by interpolating a high-resolution DEM onto the subgrid. The roughness values are  
 175 determined at the subgrid scale as well, for example by converting data from land use maps to Manning's  $n$  values and  
 176 interpolating these onto the subgrid. An example of topography and roughness on the subgrid at a velocity point is provided  
 177 in Figure 1. Specifically, the high-resolution subgrid topography and roughness values around a single velocity point  
 178 demonstrate that information from both sides (A and B) of the water level grid cell is included in calculating the flux over the  
 179 cell face  $q_{u,m,n}$  between  $z_{m,n}$  and  $z_{m+1,n}$ .



180

181 **Figure 1. High-resolution values of elevation  $z$  (panel a) and roughness  $n$  (panel b) at a U velocity point with a resolution of  $N=16 \times 16$**   
 182 **per computational cell. Colors for elevation and roughness indicate subgrid-scale values which are aggregated on the computational**  
 183 **black grid cells. Water level points are indicated by '+', while velocity points are marked with '-' and '|'.**

184

185 For each velocity point (here:  $u$ ), we distinguish between two sides A and B of a computational cell (see Figure 1). The  
 186 minimum ( $z_{b,A,min}$  and  $z_{b,B,min}$ ) and maximum ( $z_{b,A,max}$  and  $z_{b,B,max}$ ) pixel elevations at both sides are determined. The combined  
 187 minimum and maximum elevations  $z_{min}$  and  $z_{max}$  are defined as:

$$z_{min} = \max(z_{b,A,min}, z_{b,B,min}) \quad (14)$$

$$z_{max} = \max(z_{b,A,max}, z_{b,B,max}) \quad (15)$$

190

191 Values of  $\langle H_u \rangle_G$ ,  $n_u$ , and  $\varphi_u$  are now computed at discrete equidistant vertical levels, ranging between  $z_{min}$  and  $z_{max}$  as



192 :

$$193 \quad \varphi_{u,m} = \frac{1}{N} \sum_{k=1}^N p(z_m - z_{b,k}) \quad (16)$$

194 where  $p(z_m - z_k)$  is 1 for  $z_m > z_k$ , and 0 for  $z_m \leq z_k$ :

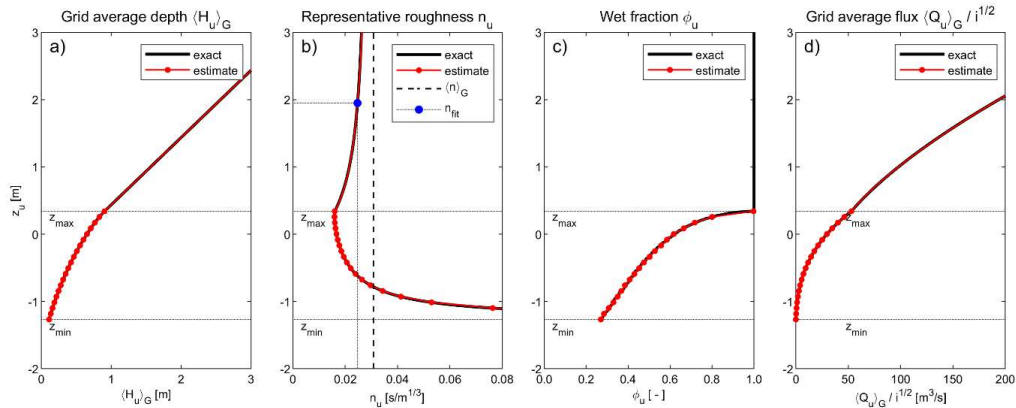
$$195 \quad \langle H_u \rangle_{G,m} = \frac{1}{N} \sum_{k=1}^N \max(z_m - z_{b,k}, 0) \quad (17)$$

$$196 \quad n_{u,m} = \frac{\langle H_u \rangle_{G,m}^{5/3}}{\frac{1}{N} \sum_{k=1}^N \left( \max(z_m - \max(z_{b,k}, z_{min}), 0) / n_k \right)^{5/3}} \quad (18)$$

197 The number ( $M$ ) of discrete vertical levels is defined by the user. We have found that around 20 levels are typically sufficient  
 198 to accurately describe the subgrid quantities  $\langle H_u \rangle_G$ ,  $n_u$  and  $\varphi_u$  as a function of water levels between  $z_{min}$  and  $z_{max}$  and is used  
 199 throughout this paper. The vertical distance between each level is defined as  $\Delta z = (z_{max} - z_{min}) / (M - 1)$ , and the elevation of  
 200 each discrete level is  $z_m = z_{min} + (m - 1) \Delta z$  (in which  $m$  goes from 1 to  $M$ ).

201

202 The subgrid tables and resulting flux (panel d) for the velocity point depicted in Figure 1, using  $M=20$  are illustrated in Figure  
 203 2. Red markers highlight the values at the discrete vertical levels.



204

205 **Figure 2. Computation of subgrid quantities  $\langle H_u \rangle_G$  (panel a),  $n_u$  (panel b) and  $\varphi_u$  (panel c) as a function of water level  $z_u$  with 20**  
 206 **discrete vertical levels ( $M = 20$ ). The resulting flux divided by the square root of the water slope  $I$  is shown in panel d. The black line**  
 207 **shows the exact solution obtained by solving Equations 5, 10, 11 and 17. The red line shows the estimate used in the SFINCS model,**  
 208 **with (for  $z \leq z_{max}$ ) linear interpolation of look-up table values, and (for  $z > z_{max}$ ) linear increase for  $\langle H_u \rangle_G$  and fit for  $n_u$ .**

209





210 Note that in Equation 18, to determine the representative roughness, the maximum of the pixel elevation and  $z_{min}$  is used. This  
 211 is done to ensure that when the water level  $z_u$  approaches  $z_{min}$ , i.e. when the highest of two adjacent grid cells becomes dry,  $n_u$   
 212 will become very large, thereby effectively blocking flow between sides A and B. No water is allowed to flow when  $z_u$  drops  
 213 below  $z_{min}$ .

214

215 The determination of  $n_u$  for completely wet velocity points is more complicated, due to its non-linear relationship with  $z_u$  at  $z_u$   
 216  $> z_{max}$  (see Figure 2b). It would be possible to store values of  $n_u$  at many levels above  $z_{max}$  in the subgrid tables, but that could  
 217 result in too large file sizes and memory use. To avoid this, SFINCS uses the following estimation for  $n_u$  instead:

218 
$$n_u = \langle n \rangle_G - \frac{\langle n \rangle_G - n_{u,M}}{\beta(z_u - z_{max}) + 1} \quad (20)$$

219 where  $\langle n \rangle_G$  is the average Manning's n of all subgrid pixels, and  $\beta$  is a fitting coefficient (with both these parameters also  
 220 stored in the subgrid tables). The fitting coefficient  $\beta$  is determined for each velocity point as:

221 
$$\beta = \frac{\langle n \rangle_G - n_{u,M} - 1}{\langle n \rangle_G - n_{fit}} \frac{z_{fit} - z_{max}}{z_{fit} - z_{max}} \quad (21)$$

222

223 Here we have defined the level  $z_{fit}$  at  $z_{max} + (z_{max} - z_{min})$ . The value for  $n_{fit}$  at  $z_{fit}$  is determined in a manner similar to Equation  
 224 18:

225 
$$n_{fit} = \frac{(\langle H_u \rangle_{G,M} + z_{fit} - z_{max})^{5/3}}{\frac{1}{N} \sum_{k=1}^N \left( \frac{z_{fit} - \max(z_{b,k}, z_{min})}{n_k} \right)^{5/3}} \quad (22)$$

226 The estimated value for  $n_u$  above  $z_{max}$  using Equation 20 is shown in Figure 2b, with the blue marker indicating  $n_{fit}$ . In very  
 227 deep water ( $z_u \gg z_{max}$ ),  $n_u$  approaches  $\langle n \rangle_G$ , whereas for  $z_u = z_{max}$ ,  $n_u$  is equal to  $n_{u,M}$ .

228

229 The behavior of  $n_u$  in Figure 2b can seem non-intuitive. Whereas the grid average water depth  $\langle H_u \rangle_G$  has a real physical  
 230 meaning, the representative roughness  $n_u$  should not be interpreted as a physical quantity but rather as a quantity that is used  
 231 to control the flux through a velocity point, given a certain grid average water depth and water slope  $i$ . It is a function not only  
 232 of the physical subgrid roughness but also of the subgrid water depth.

233

234 As mentioned previously, SFINCS uses grid average, rather than wet average quantities. Theoretically, both options would  
 235 yield identical results. The reason to choose a grid average approach is that the wet average depth and adjusted roughness can  
 236 vary much more rapidly and irregularly with changing water levels than their grid average equivalents. As a result, many more  
 237 vertical levels in the subgrid tables would be required to accurately describe wet average quantities as a function of  $z$ . This is



238 illustrated by considering a velocity point with a subgrid topography cross-section (Figure 3a). The average water depth and  
 239 adjusted roughness as a function of water level  $z$  (Figures 3a and 3b, respectively).

240

241 At each time step the model computes the water level  $z_u$  at each velocity point using the maximum of the computed water  
 242 levels in the two adjacent cells, i.e.  $z_u = \max_{\square}(z_{s\ m,n}, z_{s\ m+1,n})$ . This value is then used to query the look-up tables to find  
 243 appropriate values of the quantities  $\langle H_u \rangle_G$ ,  $\nu$ , and  $\phi$ . For partially wet velocity points ( $z_{\min} < z_u < z_{\max}$ ), a linear interpolation  
 244 of the values in the tables is used. When the entire velocity point is wet ( $z_u \geq z_{\max}$ ), the depth  $\langle H_u \rangle_G$  increases linearly with  $z_u$ :

$$245 \quad \langle H_u \rangle_G = \langle H_u \rangle_{G,M} + z_u - z_{\max} \quad (19)$$

### 246 2.3 Subgrid corrections in the continuity equation

247 The subgrid continuity equation is written in terms of grid average fluxes as:

$$248 \quad V_{m,n}^{t+\Delta t} = V_{m,n}^t + \Delta t \left( (q_u)_{G,m-1,n}^t - (q_u)_{G,m,n}^t \right) \Delta y + \left( (q_v)_{G,m,n-1}^t - (q_v)_{G,m,n}^t \right) \Delta x + S_{m,n} \quad (23)$$

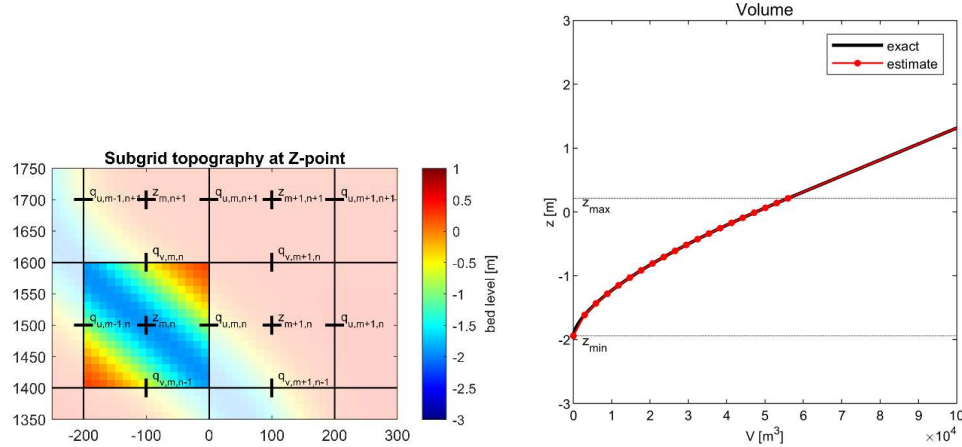
249 Contrary to Equation 2, Equation 23 computes the wet volume at the next time step, rather than the water level. The  
 250 corresponding water level  $z_s$  is obtained from the continuity subgrid tables.

251

252 To generate the subgrid tables first the minimum and maximum pixel elevations  $z_{\min}$  and  $z_{\max}$ , as well as the wet volume  $V_{\max}$   
 253 (defined as the wet volume between  $z_{\min}$  and  $z_{\max}$ ) are determined for each hydrodynamic grid cell (e.g. Figure 3). Then the  
 254 wet volume as a function of the local water level is determined:

$$255 \quad V(z) = \frac{\Delta x \Delta y}{N} \sum_{k=1}^N \max_{\square}(z - z_k, 0) \quad (24)$$

256 where  $N$  is the number of subgrid pixels in a grid cell. Finally, a number ( $M$ ) of discrete equidistant volumes are defined,  
 257 ranging between 0 and  $V_{\max}$ , where each volume is  $V_m = (m - 1) V_{\max} / (M - 1)$ . By iterating over each discrete volume  $V_m$ , we  
 258 can (using linear interpolation of Equation 24) determine the corresponding water levels  $z_s$ . An example is given in Figure 3  
 259 which shows the volumes of the highlighted cell.



260

261 **Figure 3.** Panel A: values on the subgrid-scale of elevation  $z$  at a water level point ( $N=16 \times 16$ ). Panel B. Representation of water level  
 262  $z_s$  as a function of volume  $V$  with 20 discrete volumes ( $M = 20$ ). The black line shows the exact solution of Equation 24. The red line  
 263 shows the estimate of  $z_s$  used in the SFINCS model with, for  $z_s \leq z_{max}$ , linear interpolation of look-up table values, for  $z_s > z_{max}$  a  
 264 linear increase with  $V$ .

265 During a simulation, the model computes at each time step the volume  $V$  in each cell and queries the look-up tables to find the  
 266 matching value for  $z_s$ . For partially wet cells ( $V < V_{max}$ ), a linear interpolation of the values in the tables is used. When the  
 267 entire cell is wet ( $V \geq V_{max}$ ), the water level  $z_s$  increases linearly with  $V$  and is computed as

268 
$$z_s = z_{max} + \frac{V - V_{max}}{\Delta x \Delta y} \quad (25)$$

269 Note that for pre-processing purposes, it would have been more straightforward to describe the wet volume  $V$  at equidistant  
 270 vertical levels  $z_m$  (similar to the approach for the momentum subgrid tables). However, during the simulation, the linear  
 271 interpolation of subgrid data with equidistant volume levels is much more efficient.

## 272 2.4 Pre and post-processing

273 Pre-processing steps for SFINCS include creating a mask file describing (in)active cells, interpolating bathymetry and  
 274 roughness values, and imposing boundary conditions. Tools to carry out these steps are available in both Delft Dashboard (Van  
 275 Ormondt et al., 2020) and HydroMT-SFINCS (Eilander et al., 2023 or [https://deltares.github.io/hydromt\\_sfincs/latest/](https://deltares.github.io/hydromt_sfincs/latest/)), which  
 276 both also have the capability to generate subgrid table files using high-resolution DEMs.

277

278 SFINCS stores the output of hydrodynamic quantities on the (coarse) computational grid. These results can be further  
 279 downscaled to higher-resolution flood maps at the original DEM resolution (assuming again that the computed water level in

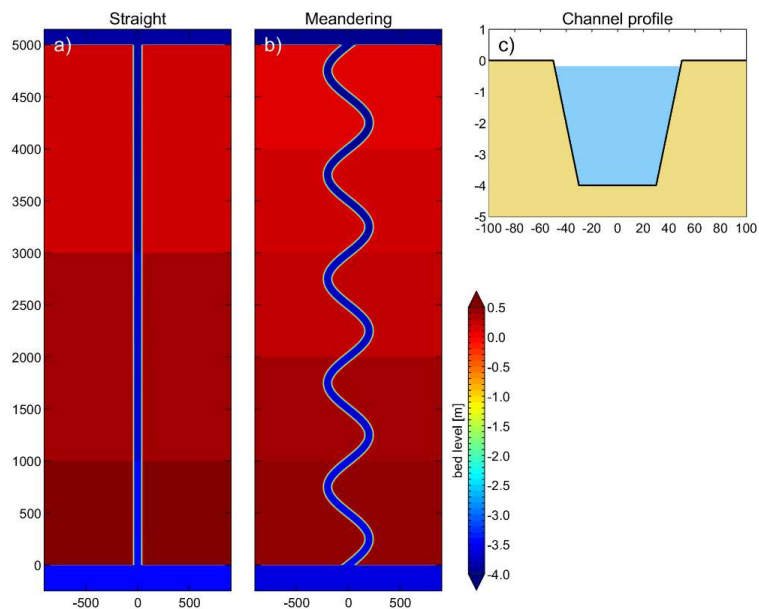


280 a grid cell is representative of each subgrid pixel within that cell). Flood depths at the DEM scale are computed by subtracting  
281 the elevation of each DEM pixel from the water level in the cell. An example of the results is presented in Figure 10.

### 282 **3 Conceptual verification cases: straight and meandering channels**

283 The first conceptual test involves a 5 km long straight channel of 100 m wide with 1:5 side slopes (Figure 4a and c), for which  
284 a synthetic bathymetry was created. The slope of the channel is  $10^{-4}$  downhill in y-direction, and the flood plains on either side  
285 of the channel have an elevation of 0.3 m above the water level in the channel. The Manning's n roughness is set to  $0.02 \text{ s/m}^{1/3}$ .  
286 Water level boundary conditions at the upstream and downstream sides are set to +0.25 m and -0.25 m, respectively, resulting  
287 in a  $10^{-4}$  water level slope, equal to the channel slope. The analytical solution, using Manning's equation for open channel flow  
288 yields a discharge of  $360 \text{ m}^3/\text{s}$ . The input files for the 5m subgrid version of this model setup can be found in Appendix B1.  
289

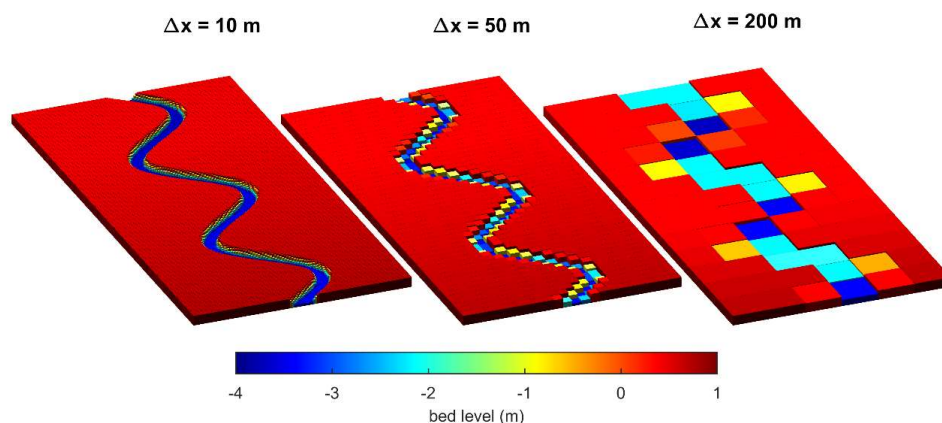
290 The second test is identical to the first, except that it has a meandering channel. The meandering channel has a sinuosity  $\Omega$  of  
291 1.32, i.e. the ratio between the length along the channel (6603 m) and its straight-line length (5000 m) (see e.g. Lazarus and  
292 Constantine, 2013 for background on river sinuosity). As the water levels upstream and downstream of the channel are kept  
293 the same, the water level slope in the meandering channel is smaller by a factor  $\Omega$ , resulting in a (lower) analytical discharge  
294 of  $313 \text{ m}^3/\text{s}$ .



295

296 **Figure 4. Schematized channel used in the conceptual verification cases, including a straight channel (top view, panel a), a**  
297 **meandering channel (top view, panel b), and a cross-section (panel c).**

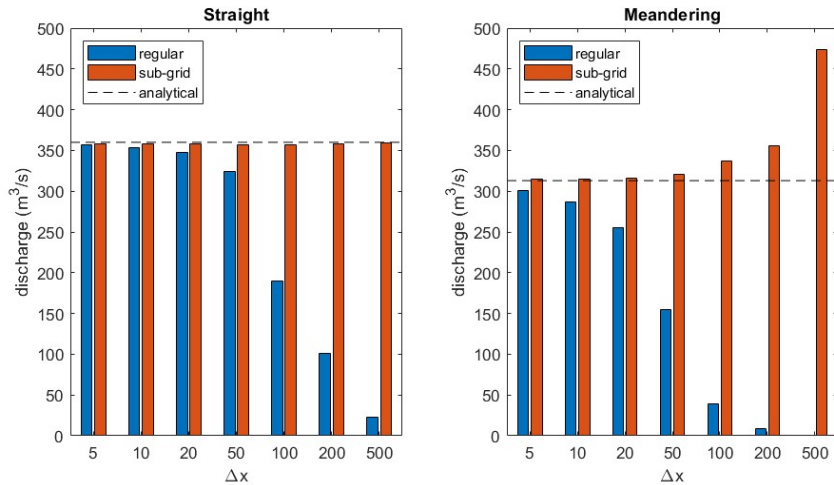
298 Simulations are carried out at various grid resolutions (5, 10, 20, 50, 100, 200, and 500 m), with both the subgrid method and  
299 regular versions of SFINCS. The subgrid simulations use a 1 m resolution subgrid, onto which the DEM is bilinearly  
300 interpolated. For the regular topography simulations, grid cell averaging is used to schematize the model bathymetry, in which  
301 the bed level of each cell is set equal to the mean of the DEM pixels within that cell. Figure 5 shows the regular model  
302 bathymetry at grid resolutions  $\Delta x$  of 10 m, 50 m, and 200 m for the meandering channel. It is clear that whereas the first two  
303 capture the channel topography reasonably well, the channel depth in the 200 m model is strongly underestimated, and its  
304 width is proportionally overestimated.



305

306 **Figure 5 Schematized meandering channel bathymetry with regular topography for hydraulic grid resolutions  $\Delta x = 10$  m,  $\Delta x = 50$**   
307 **m, and  $\Delta x = 200$  m**

308 In the first test (straight channel), the regular bathymetry models stay reasonably close to the analytical solution up to  
309 resolutions of 50m (blue bars in Figure 6 – panel A). The accuracy of the coarser models however degrades significantly with  
310 decreasing grid resolution as is to be expected. The channel depth in the coarser models is increasingly underestimated, and  
311 even though its width is proportionately overestimated, the strongly non-linear relationship between water depth and discharge  
312 results in a decrease of the discharge with decreasing grid resolution. In contrast, the discharges computed by the subgrid  
313 models are within 2% of the analytical solution across all grid resolutions (red bars in Figure 6 – panel A), proving that, at  
314 least for very simple conceptual cases, the subgrid method presented here is accurate.



315

316 **Figure 6. Effect of grid resolution  $\Delta x$  on computed discharges for regular and subgrid topography in straight (panel a) and**  
 317 **meandering (panel b) channel.**

318 In the second test (meandering channel), the trend of the regular models is similar to those in the first test (blue bars in Figure  
 319 6 – panel B), but the performance is lower than in the straight channel case, with the discharge for the two coarsest regular  
 320 models going to zero. This is caused by the fact that the hydraulic connection between some channel cells is broken in the  
 321 coarsest models (see also Figure 5).

322

323 The subgrid models in the second test show very good accuracy at resolutions up to 50 m. Coarser models start to overestimate  
 324 the discharge. The 500 m model in particular computes a discharge of 473 m<sup>3</sup>/s (an overestimation of the analytical discharge  
 325 by ~51%). There are two reasons for this: as the coarse mesh does not capture the scale of the meanders, the channel is  
 326 effectively schematized as a straight channel with a length of 5000 m. This leads to an overestimation of the true water level  
 327 slope and resulting wet average flux. Secondly, meanders inside a grid cell result in a larger wet fraction, which the model  
 328 “interprets” as a wide channel, leading to a further overestimation.

329

330 For rivers with meanders that are not resolved by the model grid, we can approximate the discharge overestimation as a function  
 331 of the channel sinuosity:

332

$$\frac{Q_m}{Q_r} = \Omega^{3/2} \quad (26)$$

333 where  $\Omega$  is the sinuosity,  $Q_r$  is the true discharge and  $Q_m$  is the discharge computed with the subgrid method (see Appendix A  
 334 for the derivation of Equation 26). Equation 26 suggests that the discharge overestimation in the 500 m subgrid model (which



335 does not resolve the meandering at all) is  $\sim 52\%$  ( $1.32^{3/2}$ ), which closely matches the computed overestimation of  $\sim 51\%$   
336 reported earlier.

## 337 4 Real-world application cases

### 338 4.1 Tidal propagation St. Johns River

339 Leijnse et al. (2021) described SFINCS model results for Hurricane Irma (2017) along the St. Johns River (Florida, USA). The  
340 length of the river is about 170 kilometers from its mouth to Lake George upstream (Figure 7 – panel A) where still a small  
341 tidal signal remains. Its width varies between 400 m and 5 km. Although the model showed good skill when compared to a  
342 full-physics Delft3D model, its 100-meter grid resolution proved insufficient to adequately propagate the tide into the estuary.  
343

344 In this test case, the St. Johns River SFINCS model from Leijnse et al. (2021) is adapted and tidal propagation into the river is  
345 simulated at several horizontal resolutions (25, 50, 100, 200, and 500 m) using both the regular and subgrid approach. The  
346 topography and bathymetry data are improved by using data obtained from the Continuously Updated Digital Elevation Model  
347 (CUDEM; CIRES, 2014). The Manning friction coefficient in the river is set to  $0.02 \text{ s/m}^{1/3}$ . The offshore boundary water levels  
348 are derived from TPXO 8.0 tidal components (Egbert and Erofeeva, 2002). Computed water levels are validated against  
349 observed tidal components from 11 tide stations (retrieved through Delft Dashboard; van Ormondt et al., 2020) (Figure 7 –  
350 panel A). The input files for the 25m subgrid version of this model setup can be found in Appendix B2.

351

352 Simulations are carried out over a one-month period to assess the model's capability to propagate the tide into the river.  
353 Analysis of the main tidal component M2 across different model variations reveals considerable differences in the upstream  
354 propagation (Figure 7B). The amplitude of M2 is approximately 75 cm at the offshore boundary and sharply decreases near  
355 the city of Jacksonville, where the river narrows significantly (about 40 kilometers upstream along the river). At 100-meter  
356 resolution, the SFINCS model with regular topography can reproduce the main trends but underestimates the tidal amplitudes  
357 relative to observations (Figure 7B), as in Leijnse et al. (2021). At the coarser 500-meter resolution, this underestimation of  
358 amplitude is significantly stronger and the tide arrives too late (Figure 7C). The tidal propagation only accurately matches the  
359 observations when utilizing a 25-meter resolution with the regular topography.

360

361 **The subgrid version of SFINCS, on the same 100-meter grid resolution, mitigates the underestimation of the regular (non-subgrid)**  
362 **version (Figure 7B). The median error of M2 amplitude prediction over the 11 observation stations decreases from 2.6 cm to 0.4 cm,**  
363 **the phase error from 4.1 to 2.1 degrees, and the overall RMSE from 8.0 to 6.4 cm (Overview of the St. Johns River near Jacksonville,**  
364 **FL, USA (Panel A), with analysis points (green dots) and tide gauges (yellow dots). Panel B: Observed (black dots) and modeled**  
365 **(colors) M2 tidal amplitudes along the river from downstream to upstream. Panel C: Observed (black dots) and modeled (colors)**  
366 **M2 tidal phases along the river. Different colors represent variations in the SFINCS model setup: red indicates the regular non-**  
367 **subgrid version, while blue denotes the subgrid version, with decreasing color intensity indicating a decrease in model resolution.**  
368 **M2 phase is converted from degrees to hours, assuming one degree equals 12.42 hours / 360 degrees. The coordinate system is WGS**  
369 **84 / UTM 15 N (EPSG 32615).**





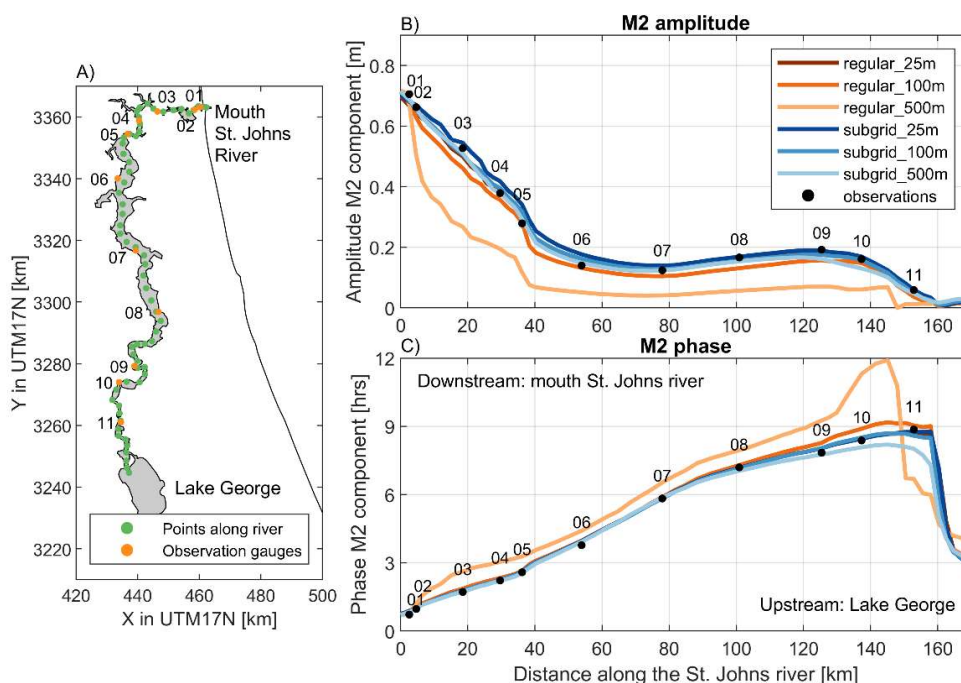
370 Table 1). Further analysis of different grid resolutions via the subgrid method illustrates that, even with coarser grid resolutions,  
371 the subgrid-enabled SFINCS version propagates the tide inland properly, even at very coarse resolutions of 500 meters. The  
372 tidal phasing is also generally more accurately resolved with subgrid versus the regular SFINCS mode.

373

374 **Computing the RMSE over the whole month tidal prediction shows that error increases from about 8 cm to about 20 cm for coarser**  
375 **grid resolutions in regular SFINCS mode (Overview of the St. Johns River near Jacksonville, FL, USA (Panel A), with analysis**  
376 **points (green dots) and tide gauges (yellow dots). Panel B: Observed (black dots) and modeled (colors) M2 tidal amplitudes along**  
377 **the river from downstream to upstream. Panel C: Observed (black dots) and modeled (colors) M2 tidal phases along the river.**  
378 **Different colors represent variations in the SFINCS model setup: red indicates the regular non-subgrid version, while blue denotes**  
379 **the subgrid version, with decreasing color intensity indicating a decrease in model resolution. M2 phase is converted from degrees**  
380 **to hours, assuming one degree equals 12.42 hours / 360 degrees. The coordinate system is WGS 84 / UTM 15 N (EPSG 32615).**



381 Table 1). However, when incorporating subgrid corrections this remains stable around this value of 8 cm. While high tide peak  
 382 predictions remain robust for the subgrid SFINCS version at larger grid resolutions (Table 1), the performance decreases more  
 383 significantly for low water peaks, indicating that during these periods, the low tide flushing of the river is still underestimated.  
 384 Integrating the subgrid raises computational costs by around 0-72% (44% on average) as a result of the extra overhead involved  
 385 in querying the subgrid tables.



386

387 **Figure 7. Overview of the St. Johns River near Jacksonville, FL, USA (Panel A), with analysis points (green dots) and tide gauges**  
 388 **(yellow dots). Panel B: Observed (black dots) and modeled (colors) M2 tidal amplitudes along the river from downstream to**  
 389 **upstream. Panel C: Observed (black dots) and modeled (colors) M2 tidal phases along the river. Different colors represent variations**  
 390 **in the SFINCS model setup: red indicates the regular non-subgrid version, while blue denotes the subgrid version, with decreasing**  
 391 **color intensity indicating a decrease in model resolution. M2 phase is converted from degrees to hours, assuming one degree equals**  
 392 **12.42 hours / 360 degrees. The coordinate system is WGS 84 / UTM 15 N (EPSG 32615).**



393 **Table 1. Overview of model skill and computational expense for evaluated scenarios of inland tidal propagation at the St. Johns**  
 394 **River, FL. Metrics include RMSE of overall difference in time-series compared to observations, RMSE of high water peaks, RMSE**  
 395 **of low water peaks, difference in M2 amplitude, and difference in M2 phase, all presented as medians over 11 observation stations.**  
 396 **The last column shows the runtime in seconds, measured on an Intel Core i9-10980XE CPU.**

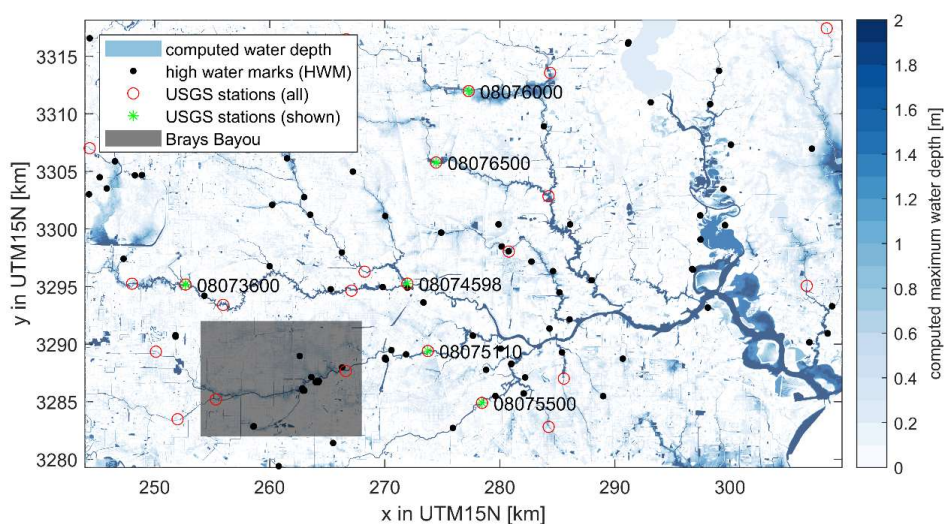
Run	RMSE overall [cm]	RMSE high water peak [cm]	RMSE low water peak [cm]	Amplitude difference M2 [cm]	Phase difference M2 [°]	Model runtime [sec]
regular_25m	7.7	6.6	9.1	-0.3	1.0	64512
regular_50m	7.8	5.7	10.1	-1.7	5.0	7596
regular_100m	8.0	4.3	12.5	-2.6	4.1	727
regular_200m	12.0	5.3	19.5	-6.7	6.5	110
regular_500m	16.1	8.3	25.4	-10.9	21.4	28
regular_1000m	20.1	14.5	-	-15.9	50.1	11
subgrid_25m	8.7	8.3	7.3	1.5	1.2	98806
subgrid_50m	7.5	7.6	6.1	0.6	1.5	12127
subgrid_100m	6.4	5.3	6.1	-0.4	2.1	1251
subgrid_200m	7.8	7.3	8.2	-1.0	1.5	159
subgrid_500m	8.2	6.6	8.7	-0.3	-1.5	28
subgrid_1000m	7.8	7.1	8.5	0.7	-4.7	15

397



398 **4.2 Pluvial flooding during Hurricane Harvey**

399 Sebastian et al. (2021) used SFINCS to hindcast the flood extent and flood depth during Hurricane Harvey (2017) in Houston,  
 400 TX. The model was validated against water level time series at 21 United States Geological Survey (USGS) observation points  
 401 and 115 high water mark (HWM) locations (Figure 8). The original model was run with a regular 25-meter resolution grid  
 402 based on a high-resolution continuous topo-bathymetry across the area of interest. The model had a fair correlation with  
 403 observed time series and HWM across the study area.



404  
 405 **Figure 8. Modeled flood inundation in the urban areas of Houston, TX, simulated with SFINCS at a 25m resolution with subgrid**  
 406 **corrections. Water depths less than 0.10 m are excluded for clarity. USGS stream gauges (red) and high-water marks (HWMs, black)**  
 407 **used for model validation are shown as solid circles. Six USGS stations, presented as time series in Figure 9, are marked with circles**  
 408 **and stars, including their station numbers. A zoom-in of the midstream portion of Brays Bayou is shown in Figure 10. The coordinate**  
 409 **system is WGS 84 / UTM 15 N (EPSG 32615). © Microsoft.**

410

411 In this field case, the model setup is adapted and flooding across Houston is simulated at several horizontal resolutions. In  
 412 particular, three variations for regular SFINCS (25, 50, and 100 meters) and 5 variations of subgrid (same resolutions as regular  
 413 mode, including 200, and 500 meters) were created. Model settings were based on Sebastian et al. (2021) model except for the  
 414 model resolution. Friction and infiltration capacity were cell-averaged from the original setup for the coarser model runs. The  
 415 input files for the 25m subgrid version of this model setup can be found in Appendix B3.

416



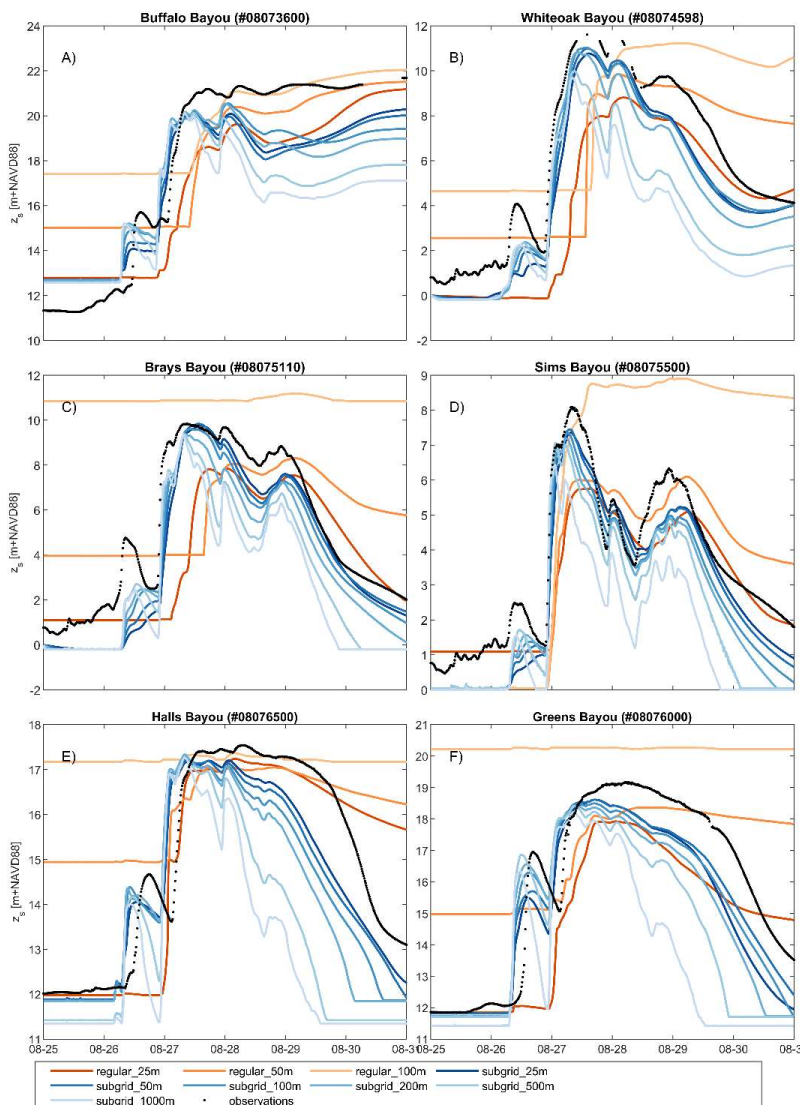
417 Almost all model versions reproduce the general shape of the observed hydrograph. However, the coarser regular version of  
418 SFINCS results in larger errors mainly due to an overestimation of the water level (Figure 9). The overestimation is driven by  
419 an incorrect representation of the bed level which is averaged across larger areas and can therefore not depict the local bayous  
420 with coarser grid cells. SFINCS with the subgrid corrections improves the model skill (Table 2). For example, when comparing  
421 the 25-meter regular with the subgrid-enabled SFINCS model with the same computational resolution, the Nash-Sutcliffe  
422 Efficiency(NSE) increases from 0.35 to 0.58. NSE is a statistical metric used to evaluate the predictive accuracy of models by  
423 comparing observed and predicted values. NSE values range from 0 to 1, with values closer to 1 indicating a better-performing  
424 model. An NSE value of 0 means the model's predictions are as accurate as using the mean of the observed data as the predictor.  
425 Model skill increases because more topo-bathymetry information is considered per grid cell via the subgrid correction in the  
426 momentum and continuity equations (see Sections 2.2 and 2.3). Despite the subgrid correction, model skill still decreases with  
427 decreasing computational resolution. For example, a 500-meter simulation with subgrid correction has an NSE close to zero.  
428 Including the subgrid feature increases computational expense by 73 to 184 % (average of 129%), because of additional  
429 overhead in querying the subgrid tables. The highest model skill is obtained with the finest model resolution (25m used here)  
430 including subgrid. Selecting the model resolution of choice is a balancing act between model skill and computational expense.  
431

432 SFINCS can store the maximum computed water level across the computational domain, with the capability to downscale this  
433 data to higher-resolution flood maps as part of a post-processing step. In particular, to calculate flood depths at the DEM scale,  
434 the elevation of individual DEM pixels is subtracted from the corresponding cell's water level (see Section 2.4). For instance,  
435 the results demonstrate that the 25-meter resolution outcomes and those downscaled to a 100-meter subgrid are quite similar.  
436 This is illustrated in Figure 10, which shows modeled flood inundation in the midstream portion of Brays Bayou using four  
437 different SFINCS model options. Panels A and C in Figure 10 highlight the comparison: Panel A presents the regular 25-meter  
438 resolution, while Panel C depicts the 'subgrid 100m – downscaled' method, which applies a downscaling method to the DEM  
439 resolution as a post-processing step. However, the 100-meter subgrid resolution runs 35 times faster than the 25-meter regular  
440 SFINCS version, while maintaining a similar level of accuracy (see Table 2) and thus, producing comparable extents of  
441 flooding. Nonetheless, it is important to note that the 100-meter resolution results tend to provide a coarser visual representation  
442 of flood extents, often overestimating them (see panels B and D in Figure A1) for both the regular and subgrid versions of  
443 SFINCS.  
444



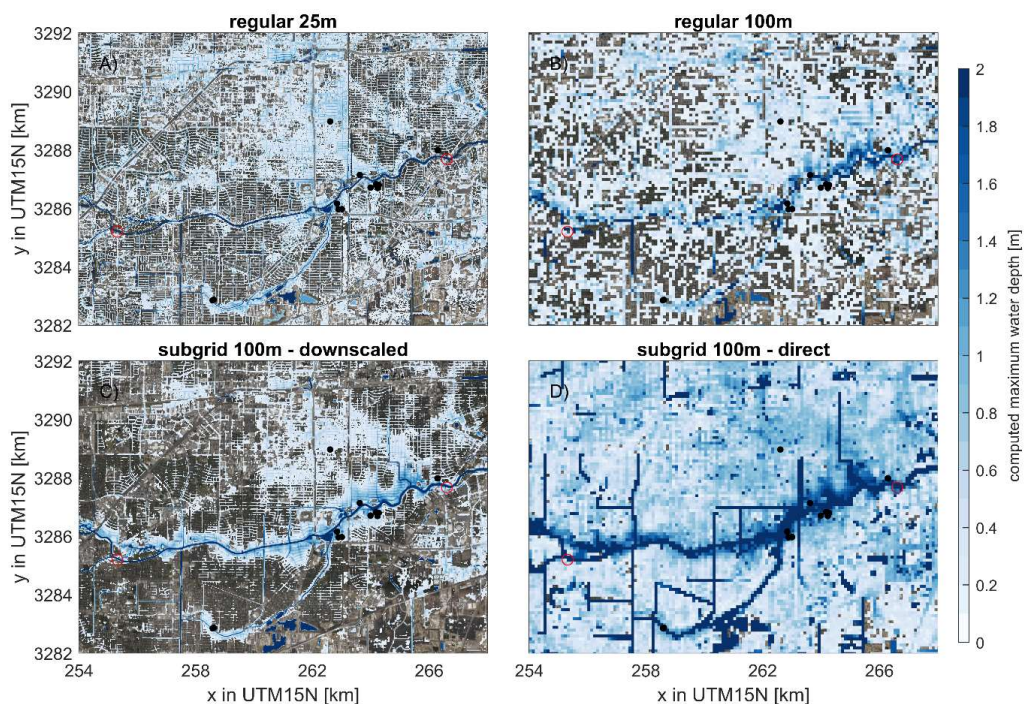
445 **Table 2. Overview of model skill and computational expense for evaluated scenarios of pluvial flooding during Harvey. Model skill**  
446 **metrics for time series, including NSE (Nash-Sutcliffe Efficiency), MAE (Mean Absolute Error), RMSE (Root Mean Square Error),**  
447 **and bias, as well as MAE for high-water marks (HWMs). The last column shows the runtime in seconds, measured on an Intel Core**  
448 **i9-10980XE CPU.**

	Time series				HWM	
simulation	NSE [-]	MAE [m]	RMSE [m]	bias [m]	MAE [m]	run time [s]
regular_25m	0.349	1.68	2.14	-0.548	0.73	12136
regular_50m	-0.007	2.08	2.58	0.405	0.68	3552
regular_100m	-1.988	3.41	3.94	2.493	0.84	116
subgrid_25m	0.581	1.29	1.58	-0.842	0.89	20951
subgrid_50m	0.540	1.3	1.57	-0.963	0.94	2801
subgrid_100m	0.495	1.35	1.62	-0.984	0.98	341
subgrid_200m	0.310	1.62	1.94	-1.226	1.09	38
subgrid_500m	0.011	2.05	2.47	-1.671	1.27	6



449

450 **Figure 9.** Overview of (computed) water levels during Hurricane Harvey. Comparison between modeled (colored lines) and observed  
 451 (black lines) hydrographs at six USGS gauge locations (labeled in Figure 8): Panels A. Buffalo Bayou (USGS 08073600); B. White  
 452 Oak Bayou at Main Street (USGS 08074598); C. Brays Bayou at MLK Jr. Blvd (USGS 08075110); D. Sims Bayou at Houston, TX  
 453 (USGS 08075500); E. Vince Bayou at Pasadena, TX (USGS 08075730); f Greens Bayou nr Houston, TX (USGS 08076000). Different  
 454 colors represent variations in the SFINCS model setup. Red is used for the regular version of SFINCS (non-subgrid). Blue is used  
 455 for the subgrid version of SFINCS. Decreasing color intensity depicts a decrease in model resolution.



456

457 **Figure 10. Modeled flood inundation in the midstream portion of Brays Bayou for 4 different SFINCS model options: A) regular**  
458 **25m, b) regular 100m, c) ‘subgrid 100m – downscaled’ is using the same model simulation as ‘subgrid 100m – direct’ (panel D), but**  
459 **then applying a downscaling method to the DEM resolution as a post-processing step. Water depths less than 0.10 m have been**  
460 **excluded for visual purposes. The locations of USGS stream gauges (red) and HWMs (black) used for the model validation are shown**  
461 **as solid circles. The coordinate system of this figure is WGS 84 / UTM 15 N (EPSG 32615). © Microsoft.**

462





## 463 5 Discussion

464 The integration of subgrid corrections into SFINCS has led to significant enhancements in accuracy, as evidenced in both  
465 conceptual verification cases (Section 3) and real-world scenarios, including tidal propagation (Section 4.1) and pluvial  
466 flooding (Section 4.2). This section delves into the impact of these accuracy enhancements and outlines the remaining  
467 challenges and areas for future research, particularly concerning flow-blocking features and the overestimation of fluxes in  
468 meandering systems.

469

470 The ability to achieve improved accuracy on the same grid resolution signifies progress. However, in practical terms, a more  
471 accurate simulation also allows for the use of coarser model resolutions. This is particularly advantageous given SFINCS's  
472 explicit numerical scheme, enabling faster and thus more efficient compound flood modeling. For example, in the real-world  
473 application cases of tidal propagation (Section 4.1) and pluvial flooding (Section 4.2), a subgrid model at 100-meter resolution  
474 demonstrates comparable, if not higher, performance to the regular 25-meter resolution SFINCS model. However, the  
475 computational cost is significantly lower with a factor of 35 to 50 speedup. The introduction of subgrid corrections does  
476 introduce additional computational expenses versus regular SFINCS. For identical model resolutions, the inclusion of subgrid  
477 corrections for momentum and continuity results in an increase in computational costs by 44 to 129%.

478

479 The downscaling routines implemented also allowed for the use of the high-resolution data in the post-processing step.  
480 However, the simple subtraction of the computed water level and high-resolution topography (introduced in Section 2.4 and  
481 applied in Section 4.2) might result in water in an area that would not be flooded using high-resolution models. While this  
482 might not affect the accuracy compared to water level stations, it does influence results and flood extents. In particular,  
483 disconnected grid cells might pop up behind levees and other flow-breaking features which form a challenge when  
484 communicating the results to stakeholders. Moreover, the presented downscaling routine has limited use for areas with steep  
485 gradients where the assumption of a constant water level per computational cell is invalid. Therefore, exploring more  
486 sophisticated hybrid surrogate models might improve the dynamic evolution of the flood extent (Fraehr et al., 2022).

487

488 Addressing subgrid connectivity poses a significant challenge for the implementation described in this paper and the broader  
489 modeling community. In contrast to approaches that relied on cell and edge clones (Begmohammadi et al., 2021) or artificial  
490 diffusion (Rong et al., 2023), SFINCS employs a subgrid weir formulation. This formulation, which is applied snapped to the  
491 grid, controls the flow between two cells but requires the creation of subgrid features during a pre-processing phase. To date,  
492 these features have been manually identified. However, there is ongoing research into algorithms capable of detecting flow-  
493 blocking features as well as the integration of methods from existing literature or direct modifications to the subgrid lookup  
494 tables to account for this.

495



496 Similarly, the overestimation of fluxes in situations with unresolved meanders continues to be a challenge. This issue is not  
497 exclusive to SFINCS's implementation of subgrid corrections but is a common challenge across subgrid modeling. Various  
498 estimates for the sinuosity  $\Omega$  have been reported in scientific literature. Lazarus and Constantine (2013) suggest that the typical  
499 range for  $\Omega$  lies between 1 and 3, where 1 corresponds to a straight channel and 3 represents the upper limit for natural, freely  
500 migrating meandering rivers. Hence, when using a computational grid that does not resolve the river meanders, the presented  
501 subgrid approach may overestimate discharges by more than a factor of 5 (or  $3^{3/2}$ ). To avoid this, it is recommended that the  
502 grid spacing of the computational grid does not exceed the width of the river channel.

## 503 6 Conclusions

504 Large-scale flood models require high accuracy at acceptable computational times. One strategy to achieve this is to use  
505 information available at a higher resolution than the hydrodynamic grid resolution in models through subgrid corrections. This  
506 paper describes a set of subgrid corrections to the Linear Inertial Equations (LIE) using grid average quantities (depth,  
507 representative roughness, wet fraction, and flux to the momentum equations and for the wet volume in the continuity equation)  
508 which were implemented in SFINCS. The model uses pre-processed subgrid tables that correlate water levels with  
509 hydrodynamic quantities by assuming constant water levels for all subgrid pixels.

510

511 The conceptual case of a straight channel showed good skill in terms of discharge fluxes with the subgrid model regardless of  
512 the model resolution while the accuracy of the regular models without subgrid correction decreased significantly with  
513 decreasing resolution. For the meandering channel differences start to emerge for coarser model resolutions with and without  
514 subgrid corrections. In particular, the difference in discharge estimation was overestimated by 50% for the coarsest subgrid  
515 model used. The ratio between the length along the channel and its straight-line length (also known as sinuosity or  $\Omega$ ) served  
516 as a valuable metric for quantifying flux overestimations. The conceptual cases gave confidence that the corrections were  
517 correctly implemented while also highlighting their limitations in grids that do not adequately resolve river meanders. In  
518 particular, we introduced an equation that allows for approximation of the discharge overestimation as a function of the channel  
519 sinuosity:

520

521 Real-world application cases further validated the subgrid corrections' benefits. For tidal propagation in the St. Johns River,  
522 the subgrid model with a 500-meter resolution matched the accuracy of the 25-meter standard SFINCS model. Similarly, in  
523 modeling pluvial flooding during Hurricane Harvey, a 25-meter resolution SFINCS model was necessary to achieve a Nash–  
524 Sutcliffe Efficiency (NSE) of 0.35, while the subgrid variant at the same resolution outperformed this with an NSE of 0.58  
525 (where a score of 1 would be perfect) and maintained comparable accuracy even at a coarser 100-meter resolution. Overall,  
526 the implementation of subgrid corrections for LIE within SFINCS shows promise for enhancing model accuracy and reducing



527 computational demands in compound flooding simulations, marking a significant step forward in the field of hydrodynamic  
528 modeling.

529

530 *Code and data availability.*

531 The SFINCS code is freely available to anyone and published on Zenodo (<https://zenodo.org/doi/10.5281/zenodo.8038533>)

532 and GitHub (<https://github.com/Deltares/SFINCS>).

533

534 *Author contributions.*

535 MO is the primary developer of the SFINCS model. KN, RG, and TL have actively contributed to the development of the

536 model. AvD initiated and co-wrote this paper. All authors were actively involved in the interpretation of the model outcomes

537 and the writing process.

538

539 *Competing interests.*

540 The authors declare that they have no conflict of interest.

541

542 *Acknowledgments and financial support*

543 We acknowledge the Deltares research program "Natural Hazards" which has provided funding to develop the model and write

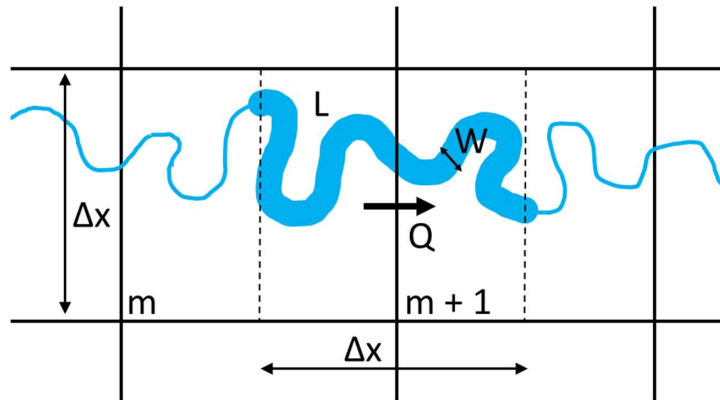
544 this paper.



545 **Appendices**

546 **Appendix A: Derivation of discharge overestimation due to unresolved meandering**

547 The subgrid approach presented in this paper may result in an overestimation of fluxes between grid cells in places where river  
 548 meanders are not sufficiently resolved by the computational grid. The overestimation may be expressed as the ratio between  
 549 the computed and theoretical fluxes. In this appendix, we describe a simple relation between this ratio and the river sinuosity  
 550 in cases where the model grid does not resolve the meanders at all. The sinuosity is defined as the ratio between the length  
 551 along the channel and its straight-line length (e.g. Lazarus and Constantine, 2013).



552  
 553 **Figure A1. Conceptual figure of the sinuosity which is defined as the ratio between the length along the channel and its straight-**  
 554 **line length**

555 Using Manning’s formula, the theoretical discharge can be described with:

556 
$$Q_r = \frac{W \sqrt{\frac{\Delta z}{L}} H^{5/3}}{n} \tag{A.1}$$

557 where W is the river width, L is the length of the center line of river stretch, Δz is the water level difference over the river  
 558 stretch, H is the channel depth (assumed uniform), and n is the Manning’s roughness coefficient.

559 Inside a model using the subgrid method, the discharge computed at the cell interface will be:

560 
$$Q_m = \Delta x \frac{\varphi \sqrt{\frac{\Delta z}{\Delta x}} H^{5/3}}{n} \tag{A.2}$$

561 where Δx is the grid size, φ is the wet fraction of the velocity point, and H is the “wet-average” depth.

562 We assume here that the sinuosity is:

563 
$$\Omega = \frac{L}{\Delta x} \tag{A.3}$$

564 Furthermore, the wet fraction φ in A.2 can be written defined as the river area W x L divided by the cell area:



565 
$$\varphi = \frac{WL}{\Delta x^2} = \frac{W}{\Delta x} \Omega \quad (A.4)$$

566 After substituting  $\varphi$  in Eq. A.2 with Eq. A.4, we can write the overestimation (i.e. the ratio of the computed and theoretical  
567 discharge  $Q_m / Q_r$ ) as:

568 
$$\frac{Q_m}{Q_r} = \frac{\frac{W}{\Delta x} \Omega \frac{\sqrt{\Delta z}}{\Delta x} H^{5/3}}{\frac{W}{n} \frac{\sqrt{\Delta z}}{L} H^{5/3}} = \Omega \sqrt{\frac{L}{\Delta x}} = \Omega \sqrt{\Omega} = \Omega^{3/2} \quad (A.5)$$



569 **Appendix B: Input files for cases considered in this manuscript**

570 **Conceptual verification cases: straight and meandering channels**

```
571 mmax      = 11
572 nmax      = 26
573 dx        = 200
574 dy        = 200
575 x0        = -1000
576 y0        = 0
577 rotation  = 0
578 latitude  = 0
579 crsgeo    = 0
580 tref      = 20190101 000000
581 tstart    = 20190101 000000
582 tstop     = 20190103 000000
583 tspinup   = 60
584 dtmapout  = 86400
585 dthisout  = 600
586 dtmaxout  = 3600
587 dtwnd     = 1800
588 alpha     = 0.5
589 theta     = 0.95
590 huthresh  = 0.005
591 manning   = 0.02
592 manning_land = 0.02
593 manning_sea = 0.02
594 rgh_lev_land = 0
595 zsini     = 1
596 qinf      = 0
597 rhoa     = 1.25
598 rhow     = 1024
599 dtmax    = 999
600 maxlev   = 999
601 bndtype  = 1
602 advection = 0
603 baro     = 0
604 pavbnd  = 0
605 gapres  = 101200
606 advlim  = 5
607 stopdepth = 100
608 depfile  = sfincs.dep
609 mskfile  = sfincs.msk
610 indexfile = sfincs.ind
611 bndfile  = sfincs.bnd
612 bzsfiler = sfincs.bzs
613 srcfile  = sfincs.src
614 disfile  = sfincs.dis
615 sbgfile  = sfincs.sbg
616 obsfile  = sfincs.obs
```



```
617 crsfile      = sfincs.crs
618 manningfile  = sfincs.manning
619 inputformat  = bin
620 outputformat = net
621 cdnrb        = 3
622 cdwnd        = 0 28 50
623 cdval        = 0.001 0.0025 0.0015
624 hmaxfile     = hmax.txt
625 zsfile       = zs.txt
626 dtout        = 3600
627 dttype       = min
628 storevelocity = 1
629 storevel     = 1
```

### 630 Tidal propagation St. Johns River

```
631 mmax         = 2720
632 nmax         = 5520
633 dx           = 25
634 dy           = 25
635 x0           = 459437.0
636 y0           = 3375791.0
637 rotation    = -164.0
638 epsg         = 32617
639 latitude     = 0.0
640 tref         = 20180901 000000
641 tstart       = 20180901 000000
642 tstop        = 20180931 000000
643 tspinup     = 60.0
644 dtout        = 86400
645 dthisout     = 600.0
646 dtrstout    = 0.0
647 dtmaxout    = 9999999999
648 trstout     = -999.0
649 dtwnd       = 1800.0
650 alpha        = 0.5
651 theta        = 1.0
652 huthresh     = 0.01
653 manning      = 0.04
654 manning_land = 0.04
655 manning_sea = 0.02
656 rgh_lev_land = 0.0
657 zsini        = 0.0
658 qinf         = 0.0
659 rhoa         = 1.25
660 rhow         = 1024.0
661 dtmax        = 60.0
662 advection    = 2
663 baro         = 0
664 pavbnd      = 0
```



```
665 gapres      = 101200.0
666 stopdepth   = 100.0
667 crsgeo      = 0
668 btfilter    = 60.0
669 viscosity   = 1
670 depfile     = sfincs.dep
671 mskfile     = sfincs.msk
672 indexfile   = sfincs.ind
673 bndfile     = ../../setup/sfincs.bnd
674 bzsfiler    = ../../setup/sfincs.bzs
675 sbgfile     = sfincs_subgrid.nc
676 obsfile     = ../../setup/noaa_xtide_v4_added_debug_points.obs
677 inputformat = bin
678 outputformat = net
679 cdnrb       = 3
680 cdwnd       = 0.0 28.0 50.0
681 cdval       = 0.001 0.0025 0.0015
```

#### 682 Conceptual verification cases: straight and meandering channels

```
683 mmax        = 2632
684 nmax        = 1555
685 dx          = 25
686 dy          = 25
687 x0          = 243943.538
688 y0          = 3279280.3807
689 rotation    = 0
690 epsg        = 32615
691 tref        = 20170825 000000
692 tstart      = 20170825 000000
693 tstop       = 20170831 000000
694 dtout       = 86400
695 dthisout    = 600
696 dtmaxout    = 518400
697 dtwnd       = 600
698 alpha       = 0.5
699 theta       = 1
700 huthresh    = 0.05
701 rgh_lev_land = 0
702 zsini       = 0
703 qinf        = 0
704 rhoa        = 1.25
705 rhow        = 1000
706 advection   = 1
707 stopdepth   = 9999
708 depfile     = sfincs.dep
709 mskfile     = sfincs.msk
710 indexfile   = sfincs.ind
711 bndfile     = sfincs.bnd
712 bzsfiler    = sfincs.bzs
```





```
713 srcfile      = sfincs.src
714 disfile      = sfincs.dis
715 sbgfile      = sfincs_subgrid.nc
716 amprfile     = Observations_Interpolate_600x600_halfhour_test.amr
717 obsfile      = sfincs.obs
718 inputformat  = bin
719 outputformat = net
720 cd_nr        = 0
721 geomskfile   = sfincs.gms
722 hmaxfile     = hmax.dat
723 hmaxgeofile  = hmaxgeo.dat
724 zsfile       = zs.dat
725 vmaxfile     = vmax.dat
726 qinffile     = qinf_constanttime_spatialvary
727 storevel     = 1
728
```



## 729 References

- 730 Bates, P. D., Horritt, M. S., & Fewtrell, T. J. (2010). A simple inertial formulation of the shallow water equations for efficient  
731 two-dimensional flood inundation modelling. *Journal of Hydrology*, 387(1–2), 33–45.  
732 <https://doi.org/10.1016/j.jhydrol.2010.03.027>
- 733 Begmohammadi, A., Wirasaet, D., Poisson, A., Woodruff, J. L., Dietrich, J. C., Bolster, D., & Kennedy, A. B. (2023).  
734 Numerical extensions to incorporate subgrid corrections in an established storm surge model. *Coastal Engineering*  
735 *Journal*, 65(2), 175–197. <https://doi.org/10.1080/21664250.2022.2159290>
- 736 Begmohammadi, A., Wirasaet, D., Silver, Z., Bolster, D., Kennedy, A. B., & Dietrich, J. C. (2021). Subgrid surface  
737 connectivity for storm surge modeling. *Advances in Water Resources*, 153, 103939.  
738 <https://doi.org/10.1016/j.advwatres.2021.103939>
- 739 Casulli, V. (2009). A high-resolution wetting and drying algorithm for free-surface hydrodynamics. *International Journal for*  
740 *Numerical Methods in Fluids*, 60(4), 391–408. <https://doi.org/10.1002/flid.1896>
- 741 CIRES. (2014). Cooperative Institute for Research in Environmental Sciences (CIRES) at the University of Colorado, Boulder.  
742 2014: Continuously Updated Digital Elevation Model (CUDEM). Accessed 6/30/21. <https://doi.org/10.25921/ds9v-ky35>
- 743 Defina, A. (2000). Two-dimensional shallow flow equations for partially dry areas. *Water Resources Research*, 36(11), 3251–  
744 3264. <https://doi.org/10.1029/2000WR900167>
- 745 Didier, D., Caulet, C., Bandet, M., Bernatchez, P., Dumont, D., Augereau, E., Floe'h, F., & Delacourt, C. (2020). Wave runup  
746 parameterization for sandy, gravel and platform beaches in a fetch-limited, large estuarine system. *Continental Shelf*  
747 *Research*, 192, 104024. <https://doi.org/10.1016/j.csr.2019.104024>
- 748 Egbert, G. D., & Erofeeva, S. Y. (2002). Efficient inverse modeling of barotropic ocean tides. *Journal of Atmospheric and*  
749 *Oceanic Technology*, 19(2), 183–204. [https://doi.org/10.1175/1520-0426\(2002\)019<0183:EIMOBO>2.0.CO;2](https://doi.org/10.1175/1520-0426(2002)019<0183:EIMOBO>2.0.CO;2)
- 750 Eilander, D., Couasnon, A., Leijnse, T., Ikeuchi, H., Yamazaki, D., Muis, S., Dullaart, J., Haag, A., Winsemius, H. C., &  
751 Ward, P. J. (2023). A globally applicable framework for compound flood hazard modeling. *Natural Hazards and Earth*  
752 *System Sciences*, 23(2), 823–846. <https://doi.org/10.5194/nhess-23-823-2023>
- 753 Jelesnianski, C. P. ., Chen, J., & Shaffer, W. A. . (1992). SLOSH : Sea, Lake, and Overland Surges from Hurricanes. NOAA  
754 Technical Report, April.
- 755 Kennedy, A. B., Wirasaet, D., Begmohammadi, A., Sherman, T., Bolster, D., & Dietrich, J. C. (2019). Subgrid theory for  
756 storm surge modeling. *Ocean Modelling*, 144, 101491. <https://doi.org/10.1016/j.ocemod.2019.101491>
- 757 Lazarus, E. D., & Constantine, J. A. (2013). Generic theory for channel sinuosity. *Proceedings of the National Academy of*  
758 *Sciences*, 110(21), 8447–8452. <https://doi.org/10.1073/pnas.1214074110>
- 759 Leijnse, T., van Ormondt, M., Nederhoff, K., & van Dongeren, A. (2021). Modeling compound flooding in coastal systems  
760 using a computationally efficient reduced-physics solver: Including fluvial, pluvial, tidal, wind- and wave-driven  
761 processes. *Coastal Engineering*, 163, 103796. <https://doi.org/https://doi.org/10.1016/j.coastaleng.2020.103796>
- 762 Lesser, G. R., Roelvink, D., van Kester, J. a. T. M., & Stelling, G. S. (2004). Development and validation of a three-dimensional



- 763 morphological model. *Coastal Engineering*, 51(8–9), 883–915. <https://doi.org/10.1016/j.coastaleng.2004.07.014>
- 764 Luettich, R. A., Westerink, J. J., & Scheffner, N. W. (1992). ADCIRC: An Advanced Three-Dimensional Circulation Model  
765 for Shelves Coasts and Estuaries, Report 1: Theory and Methodology of ADCIRC-2DDI and ADCIRC-3DL, Dredging  
766 Research Program Technical Report DRP-92-6. In Coastal Engineering Research Center (U.S.), Engineer Research and  
767 Development Center (U.S.). (Issue 32466, pp. 1–137). <https://erdc-library.erdc.dren.mil/jspui/handle/11681/4618>
- 768 McGranahan, G., Balk, D., & Anderson, B. (2007). The rising tide: assessing the risks of climate change and human settlements  
769 in low elevation coastal zones. *Environment and Urbanization*, 19(1), 17–37.  
770 <https://doi.org/10.1177/0956247807076960>
- 771 Ramirez, J. A., Rajasekar, U., Patel, D. P., Coulthard, T. J., & Keiler, M. (2016). Flood modeling can make a difference:  
772 Disaster risk-reduction and resilience-building in urban areas. *Hydrology and Earth System Sciences Discussions*,  
773 November, 1–21. <https://doi.org/10.5194/hess-2016-544>
- 774 Rong, Y., Bates, P., & Neal, J. (2023). An improved subgrid channel model with upwind-form artificial diffusion for river  
775 hydrodynamics and floodplain inundation simulation. *Geoscientific Model Development*, 16(11), 3291–3311.  
776 <https://doi.org/10.5194/gmd-16-3291-2023>
- 777 Sebastian, A., Bader, D. J., Nederhoff, K., Leijnse, T., Bricker, J. D., & Aarninkhof, S. G. J. (2021). Hindcast of pluvial, fluvial  
778 and coastal flood damage in Houston, TX during Hurricane Harvey (2017) using SFINCS. *Natural Hazards*, 2017.  
779 <https://doi.org/10.1007/s11069-021-04922-3>
- 780 Sehili, A., Lang, G., & Lippert, C. (2014). High-resolution subgrid models: background, grid generation, and implementation.  
781 *Ocean Dynamics*, 64(4), 519–535. <https://doi.org/10.1007/s10236-014-0693-x>
- 782 Stelling, G. S., & Duijnmeijer, S. P. A. (2003). A staggered conservative scheme for every Froude number in rapidly varied  
783 shallow water flows. *International Journal for Numerical Methods in Fluids*, 43(12), 1329–1354.  
784 <https://doi.org/10.1002/fld.537>
- 785 van Ormondt, M., Leijnse, T., Nederhoff, K., de Goede, R., van Dongeren, A., & Tycho Bovenschen. (2023). SFINCS: Super-  
786 Fast INundation of CoastS model (2.0.3 Cauberg Release Q4 2023). Zenodo. <https://doi.org/10.5281/zenodo.10118583>
- 787 van Ormondt, M., Nederhoff, K., & Van Dongeren, A. (2020). Delft Dashboard: a quick setup tool for hydrodynamic models.  
788 *Journal of Hydroinformatics*, 22(3), 510–527. <https://doi.org/10.2166/hydro.2020.092>
- 789 Volp, N. D., Van Prooijen, B. C., & Stelling, G. S. (2013). A finite volume approach for shallow water flow accounting for  
790 high-resolution bathymetry and roughness data. *Water Resources Research*, 49(7), 4126–4135.  
791 <https://doi.org/10.1002/wrcr.20324>
- 792 Vousdoukas, M. I., Voukouvalas, E., Annunziato, A., Giardino, A., & Feyen, L. (2016). Projections of extreme storm surge  
793 levels along Europe. *Climate Dynamics*, 47(9–10), 3171–3190. <https://doi.org/10.1007/s00382-016-3019-5>
- 794 Warren, I. R., & Bach, H. K. (1992). MIKE 21: a modelling system for estuaries, coastal waters and seas. *Environmental*  
795 *Software*, 7(4), 229–240. [https://doi.org/10.1016/0266-9838\(92\)90006-P](https://doi.org/10.1016/0266-9838(92)90006-P)
- 796 Woodruff, J. L., Dietrich, J. C., Wirasat, D., Kennedy, A. B., Bolster, D., Silver, Z., Medlin, S. D., & Kolar, R. L. (2021).  
797 Subgrid corrections in finite-element modeling of storm-driven coastal flooding. *Ocean Modelling*, 167, 101887.



798 <https://doi.org/10.1016/j.ocemod.2021.101887>

799 Woodruff, J., Dietrich, J. C., Wirasaet, D., Kennedy, A. B., & Bolster, D. (2023). Storm surge predictions from ocean to  
800 subgrid scales. *Natural Hazards*, 117(3), 2989–3019. <https://doi.org/10.1007/s11069-023-05975-2>

801 Yu, D., & Lane, S. N. (2011). Interactions between subgrid-scale resolution, feature representation and grid-scale resolution  
802 in flood inundation modelling. *Hydrological Processes*, 25(1), 36–53. <https://doi.org/10.1002/hyp.7813>

803 Yu, D., & Lane, S. N. (2006). Urban fluvial flood modelling using a two-dimensional diffusion-wave treatment, part 2:  
804 development of a subgrid-scale treatment. *Hydrological Processes*, 20(7), 1567–1583. <https://doi.org/10.1002/hyp.5936>

805